

Single versus Multi-Tone Wireless Power Transfer with Physically Large Arrays

Jarne Van Mulders*, Benjamin J. B. Deutschmann[†], Geoffrey Ottoy*, Lieven De Strycker*,
Liesbet Van der Perre*, Thomas Wilding[†] and Gilles Callebaut*
*KU Leuven, Belgium, [†]Graz University of Technology, Austria

Abstract—Distributed beamforming is a key enabler to provide power wirelessly to a massive amount of energy-neutral devices (ENDs). However, without prior information and fully depleted ENDs, initially powering these devices efficiently is an open question. This work investigates and assesses the feasibility of harvesting sufficient energy to transmit a backscatter pilot signal from the END, which can be then used for coherent downlink transmission. We experimentally evaluated adaptive single-tone and multi-tone signals during initial charging. The results indicate that the response time for ENDs with unknown locations can extend to several tens of seconds. Notably, the adaptive single-tone excitation shows, among others, better performance at lower transmit power levels, providing a faster response. These findings underscore the potential of adaptive single-tone signals in optimizing power delivery to END in future networks.

Index Terms—initial access, energy-neutral device, waveform, wireless power transfer, large arrays, experimental study

I. INTRODUCTION

Radio frequency power transfer (RFPT) has seen increasing interest from both academia and industry. Applications such as logistic tags and electronic shelf labels (ESLs) can be built without batteries using advanced wireless power transfer (WPT) techniques. Future 6G networks have the potential to support such applications through distributed WPT. Energy-neutral devices (ENDs) have only limited energy storage available to buffer the required energy in order to provide a stable energy source to the device. Hence, these devices need sufficient power during the initial access phase, i.e., when the energy storage is fully depleted, to charge this buffer.

Multi-Antenna WPT. Multi-antenna systems offer far-field beamforming and near-field beamfocusing to enhance WPT efficiency at targeted devices and reduce unintended power reception. Beamforming typically relies on channel reciprocity, where the infrastructure learns the channel from an uplink pilot signal sent by the device. This information is then used to adjust the antennas' phases and amplitudes to create constructive interference at the target location. However, ENDs need to be powered before they can transmit the necessary pilot signal. Various methods have been proposed to power devices during initial access, i.e., when the energy storage is fully depleted:

- 1) Uniform Power Distribution: Phases of all antennas are randomly altered over time to achieve a quasi-uniform power distribution, as introduced in [1, 2], which smooths

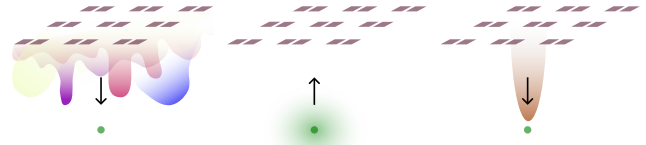


Fig. 1: Considered three-phase operation: 1) non-coherent downlink WPT (left), 2) 10-byte uplink pilot transmission (middle) and 3) reciprocity-based coherent downlink WPT (right). This work focuses on the two first phases.

the beamfocusing effect. This yields over time a superposition of the beam patterns as illustrated in phase 1 of Fig. 1.

- 2) Search Algorithms: Algorithms adjust beam weights to maximize received power. For instance, a grid search strategy along the x- and y-axes of the planar array is used in [3]. To reduce search time, [4] employs orthogonal bases to change phases of multiple antenna elements simultaneously, sweeping the phases of antenna groups while recording received power. This technique does not require array calibration or prior knowledge of the environment.
- 3) Position-Based WPT: Proposed in [2, 5], this method predicts geometry-based channel state information (CSI) using prior position and environment information. In [5], geometry-based planar and spherical wavefront beamformers are compared to reciprocity-based beamformers using data from an XL-MIMO testbed.
- 4) (Prior) Channel-Based WPT: This approach optimizes WPT efficiency using previously obtained CSI or partial CSI. For instance, [6] explores non-coherent and coherent beamforming strategies for initial access using partial CSI.

Single-Tone and Multi-Tone Excitation. Multi-tone techniques are being proposed in literature as an efficient waveform for RFPT. For instance, in [7] the CSI is exploited to allocate less power to the frequency components (tones) that have weak channel gains. In [8], the read range of a RFID tag was increased by employing a multi-tone waveform.

However, the aforementioned studies heavily rely on models, not taking into account matching circuit mismatch, different harvester architectures and other hardware impairments, all affecting the performance of the energy harvesting capabilities

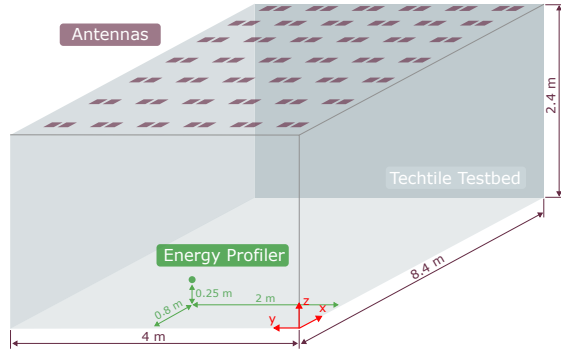


Fig. 2: Illustration of the real-life testbed [11] and energy profiler’s location.

of an END. Moreover, previously mentioned studies rely on partial CSI knowledge and an optimised phase relation between all multi-tone components, which is not possible in our case (step 1 in Fig. 1). More complex AC-to-DC converters and built-in charge pumps could potentially benefit from single-tone WPT. This belief is also challenged in [9], where the impact of multi-tone excitation on the output direct current (DC) power of a voltage-doubler FM-band RF energy harvester is examined. The findings indicate that multi-tone excitation not always enhances the DC output power.

Contributions and Findings.

In this study, we experimentally determine the most effective strategy for initially charging a real END without prior knowledge of its location and with a depleted energy supply. The considered operation is depicted in Fig. 1. A custom-developed energy profiler (EP) utilizes a state-of-the-art energy harvesting test IC from NXP. We compare the performance of single-tone and multi-tone transmissions using an 84-antenna system. Our experiments demonstrate that adaptive single-tone transmission outperforms multi-tone waveforms across all key metrics: harvester efficiency (RF-to-DC conversion), probability of achieving the required microcontroller unit (MCU) voltage, and uplink pilot response time. This indicates that single-tone transmission enables ENDS to receive more energy and wake up faster compared to multi-tone signals for initial access. The design files, along with details about the experiment and the collected data, are available in the [GitHub](#) repository [10].

II. LARGE ARRAY, ENERGY-NEUTRAL DEVICE AND ENERGY PROFILER

Performing an empirical comparison between several transmit signals involves numerous hardware and software requirements. This section outlines the developments necessary for conducting practical measurements. Some components are not commercially available and were specifically developed for this work. A flexible and configurable infrastructure is crucial, incorporating large arrays as introduced in Section II-A. Additionally, an energy-neutral device implementation is required to determine the necessary energy and energy buffer size, as detailed in

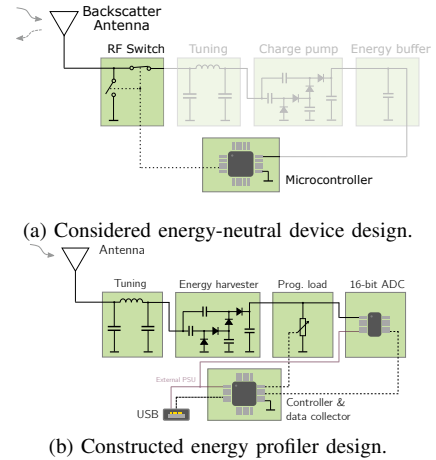


Fig. 3: Hardware architectures. The transparent blocks of the END architecture were not considered during the analysis, as the primary goal was to measure the power consumption of the MCU and the RF switch.

Section II-B. Finally, an EP is essential for performing RF-to-DC conversion and measuring the received DC energy, as explained in Section II-C.

A. Large Array

The measurements described in Section III are performed with the Techtile testbed [11]. Only parts of the infrastructure are used in this work, specifically the antennas located in the ceiling. The setup involves 84 antennas paired with 42 universal software radio peripheral (USRP) B210 devices. Control of the USRPs is managed by 42 Raspberry Pis (RPIs) units, which are connected to the local network of the Techtile testbed. The testbed is time and frequency synchronised, given that multiple USRPs could generate exactly the same frequency from a shared 10 MHz clock source. As a result, the relative phase between two frequency synchronous USRPs is constant over time. The dimensions of the testbed are illustrated in Fig. 2, and a more detailed discussion of the testbed can be found in [11].

B. Energy-Neutral Device and Energy Buffer Requirements

For coherent downlink wireless power beamforming, the infrastructure, here in form of a large array, requires CSI. In order to obtain this, the END can use backscattering. The objective of this section is to determine the energy needed at the END side to backscatter a pilot signal and, additionally, to ascertain the size of the buffer capacitor.

We consider an embedded device with only backscatter capabilities, as detailed in Fig. 3a. A low-power MCU uses one of its internal timers to control an external RF switch. The RF switch is located just behind the antenna, allowing it to change the impedance between the harvester impedance and a short-circuit termination.

The timer divides the 1.024 MHz clock by two, to provide a 512 kHz local oscillator (LO) offset to the RF switch and

therefore prevents interference with the carrier wave. A second timer modulates information at a baud rate of 1 kbit s^{-1} by controlling the first timer. We assume a pilot message of 10 bytes¹. Consequently, it takes 80 ms to backscatter 10 bytes of data. The MCU, powered at 1.8 V, consumes $380 \mu\text{W}$ during operation. Thus, the energy demand of the MCU E_{MCU} amounts $30.4 \mu\text{J}$. The data in the message being backscattered is not of interest in this work.

The MCU starts executing instructions once the voltage exceeds the threshold value $V_{\text{MCU}_{th}}$ of 1.75 V and stops executing instructions when the supply voltage drops below the brown-out threshold V_{BOD} value of 1.55 V. Subsequently, the buffer capacitor C_B can be calculated using

$$C_B = \frac{2E_{\text{MCU}}}{V_{\text{MCU}_{th}}^2 - V_{\text{BOD}}^2}. \quad (1)$$

Inserting the values from above results in a minimum buffer capacitance of $92 \mu\text{F}$ is required, which means a capacitance of $100 \mu\text{F}$ should be sufficient to send the pilot message for the considered END architecture (Fig. 3a).

C. Energy Profiler

To achieve accurate DC power measurements that account for nonlinearities and threshold voltage levels, we have developed and implemented an energy profiler (EP). The EP incorporates several features to validate and optimize the performance of RFPT systems. It includes a tuning network that enhances impedance matching with antennas having a characteristic impedance of 50Ω . The system features an energy harvester that converts RF signals into DC energy [12], capable of providing a maximum output voltage of 2 V, without damaging the internal charge pump circuits. This voltage level should be sufficient to reliably power MCUs, as discussed earlier in Section II-B. Additionally, the profiler integrates precise power measurement capabilities using a programmable potentiometer and a high-resolution 16-bit analog-to-digital converter (ADC). This setup allows for accurate monitoring of power levels, crucial for evaluating energy harvesting efficiency. Operating at a sample rate and control loop speed of 1 kHz, the EP ensures rapid response times and precise control in dynamic environments. Furthermore, the EP offers an adjustable target voltage feature, enabling users to simulate real-life conditions accurately. This flexibility is essential, as MCUs typically require a minimum input voltage of approximately 1.8 V for stable operation. By adjusting the target voltage, the EP can simulate varying operating conditions to validate performance under different scenarios effectively.

¹Although the pilot length determines the number of ENDS that can be potentially multiplexed, here we do not target simultaneous uplink pilot transmission. Actually, the hypothesis is that using adaptive single carrier transmission, ENDS will awake at different time instances, mitigating pilot contamination. Hence, the pilot length only has an effect on the channel estimate quality, which does not affect the findings and conclusions of this work.

III. MEASUREMENT CAMPAIGN

Our objective is to achieve a rapid response time (phase 2 in Fig. 1) from the END, ensuring that it transmits its pilot message as promptly as possible. Additionally, we seek to accomplish this with minimal overall transmit power from the infrastructure. Three key questions need to be addressed to optimize this process: What is the optimal signal type to apply? How should the USRPs be configured? What is the required transmit power per antenna? These questions will be systematically explored through measurements in this section and the subsequent one.

A. Measurement Setup

We consider the infrastructure depicted in Fig. 2, where the ceiling antennas are utilized for the measurements. In the measurement setup, the receiver has two antennas to compare the harvested DC power with the RF channel power, as shown in Fig. 4. The EP connected to the right antenna and explained in Section II-C, forwards the DC power and DC voltage values to a central computer at a sample rate of 250 Hz. The target voltage is set to 1.8 V with an accuracy of 50 mV, meaning that the internal regulator does not adjust the programmable load, if the harvester voltage is within the interval $[1.75, 1.85]$ V. Simultaneously, the RF channel power is measured with the left antenna and an MSO64B oscilloscope (6 GHz bandwidth) at a sample rate of approximately 20 Hz.

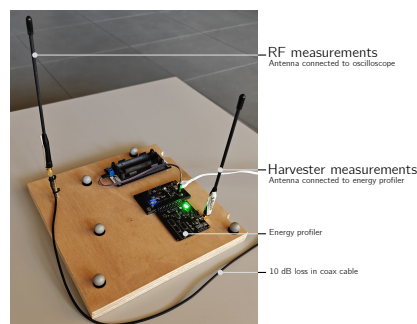


Fig. 4: Picture of the receive side of the measurement setup, showing two half-wavelength antennas and the energy profiler.

Furthermore, the measurement instruments, RPIs, and USRPs are controlled by a central computing system. This system reconfigures the infrastructure for each measurement session and ensures storage of the obtained data.

B. Conducted Measurements

The USRPs of Techtile can be configured in various ways. In this paper, we focus on two relevant configurations of the infrastructure:

Meas 1 All transmitters are frequency synchronized and configured to transmit at the same frequency, i.e., 920 MHz. To avoid the possibility of an END being located in an area of destructive interference, the phases are adjusted periodically, i.e., adaptive single-tone transmission. In this work, the phase of each antenna is randomly changed every 5 seconds.

Meas 2 The harvester’s bandwidth spans several MHz, allowing it to harvest frequency components adjacent to the center frequency of 920 MHz. Consequently, a second configuration involves generating an equally-spaced multi-tone excitation by assigning individual frequencies to each antenna. Here, a frequency offset of 100 Hz is used. Using 84 antennas, this equates to 84 carriers, spanning a bandwidth of 8.4 kHz.²

Since the END’s location is often unknown in real-world scenarios, all antennas are configured with the same gain setting for each USRP. If the location were known, an optimization algorithm could be employed to efficiently transfer the initial energy to the END, as proposed in [6] (Section I).

The transmit gain of the 84 antennas is swept from 75 dB to 85 dB in 1 dB increments, corresponding to a real output power range of 9.1 to 17.4 dBm per antenna. This varying gain is expected to demonstrate the nonlinearities of the harvester, allowing to determine the required gain (or equivalently transmit power) necessary to provide sufficient initial energy to the END. In total, 11 gain configurations are tested per measurement, each with a duration of 30 minutes.

All measurements are conducted at a static location (Fig. 2). It is important to note that the locations of the two antennas are not identical, thus the antennas will experience different small-scale fading. However, the average received RF and DC powers are still relevant for comparison purposes, as discussed in Section IV. The location of the receiver in our measurement setup remained unchanged in this study (Fig. 2).

IV. DATA PROCESSING AND DISCUSSION

In this section, we demonstrate that for the same amount of radiated power, single-tone excitation yields better harvester efficiency and increases the likelihood of receiving a response. A detailed discussion is provided in this section.

A. Average RF/DC Energy and Harvester Efficiency

Due to the distance between the scope and EP antenna, the received power is different at both locations due to small-scale fading effects, as previously mentioned in Section III-B. For each individual measurement, such as those shown in Figs. 6a and 6b, the average RF and DC power is determined over the entire measurement duration. The relationship between these two results indicates the harvester efficiency. The average RF and DC power levels, as well as efficiency metrics for both single-tone and multi-tone excitation, are plotted in Fig. 5.

The results from our experiments indicate that single-tone excitation yields higher efficiency values compared to multi-tone excitation. This improvement is attributable to the higher measured average DC power (per USRP gain) observed for single-tone signals. As expected, the average RF power (represented by the black lines) remains approximately constant across both excitation modes. This consistency arises because the differences between the transmitted signals—namely, the

²In contrast to other work, our setup uses single carrier transmission per antenna resulting in a received signal with frequency fading due to different channels between the distributed transmit antennas and the END even though a narrowband signal is transmitted.

frequency offsets and periodic phase adjustments—do not cause significant variations in the average RF channel power.

In these measurements, the total transmitted power is defined by the number of antennas and the transmit power. The overall efficiency is presented in Table I.

TABLE I: Overall efficiency levels and feasibility of the target voltage for various transmit power levels, with V_{th} equals $V_{MCU_{th}}$.

USRP		Total	Single-tone signal		Multi-tone signal	
gain [dB]	power [dBm]	power [dBm]	Efficiency [ppm]	$V_B > V_{th}$ [%]	Efficiency [ppm]	$V_B > V_{th}$ [%]
75	9.1	28.34	0.8	2.5	0.7	0.0
76	9.96	29.2	0.8	2.77	0.8	0.0
77	10.82	30.06	1.2	8.01	0.9	0.0
78	11.68	30.92	1.3	11.54	1.0	0.59
79	12.54	31.78	1.6	18.87	1.1	1.93
80	13.4	32.64	1.9	27.59	1.2	14.98
81	14.2	33.44	2.1	37.52	1.2	31.39
82	15.0	34.24	2.3	43.01	1.2	50.66
83	15.8	35.04	2.2	44.8	1.2	57.34
84	16.6	35.84	2.7	53.69	1.6	57.95
85	17.4	36.64	2.7	62.08	1.7	53.91

B. Feasibility of the Target Voltage

One of the key questions is whether the harvested DC power provides sufficient voltage for the MCU to wake-up and stay active long enough to transmit an uplink pilot. Therefore, the initial study evaluates whether the harvested voltage level exceeds the 1.75 V threshold ($V_{MCU_{th}}$). This voltage level is measured by the EP. Table I indicates that at lower USRP gain levels, the harvested voltage in multi-tone measurements does not consistently exceed $V_{MCU_{th}}$. In contrast, single-tone signals exhibit a higher probability of surpassing this threshold, particularly at lower transmit power levels.

C. Estimation of the END Response Time

One of the main contributions of this manuscript is to provide insights into the response time of the END. Based on this information, it is feasible to estimate how long the infrastructure needs to remain actively listening for backscattered signals. Section II-B defined an END buffer of 100 μ F that should be charged to $V_{MCU_{th}}$ to transmit the pilot message. To proceed with the response time calculations, the voltage profile across the buffer must be known. Section IV-C1 explains how the results from Section III can be processed to estimate the voltage profile across the capacitor. Section IV-C2 analyzes whether the buffer voltage effectively reaches the desired voltage levels.

1) *Estimated Time to Charge an END Buffer:* The buffer voltage $V_B(t)$ is calculated according to

$$V_B(t) = \sum_{n=1}^{t/\Delta t} V_{B_n} \quad \text{for } t/\Delta t \leq N \quad (2)$$

with V_{B_n} the voltage after processing n samples and N the number of data samples available in the EP dataset. The time interval Δt depends on the EP sampling rate. The instantaneous change in energy $\Delta E_{B_n} = P_{B_n} \Delta t$ is computed according to

$$\Delta E_{B_n} = \frac{1}{2} C_B \left(V_{B_n}^2 - V_{B_{n-1}}^2 \right). \quad (3)$$

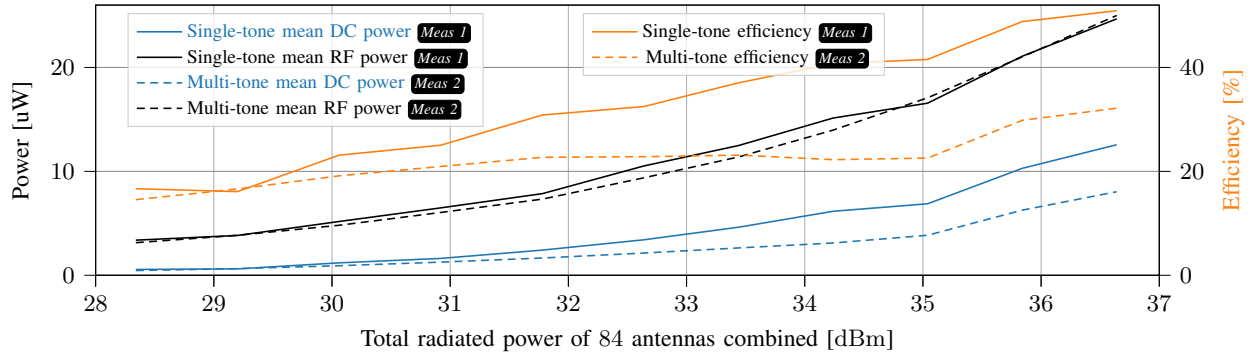


Fig. 5: Average power levels and corresponding efficiency levels of the harvester. The plot illustrates the relationship between average RF input- and DC output-power across the energy harvester. The adaptive single-tone configuration achieves, on average, higher efficiency levels.

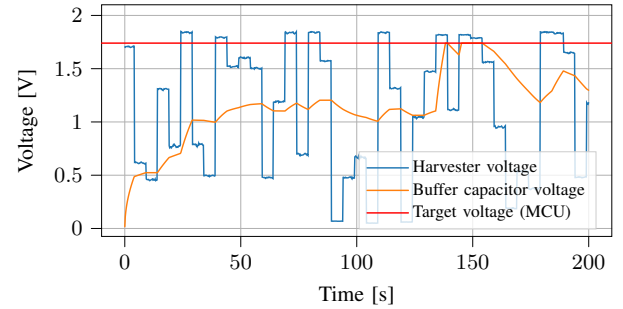
The total power supplied to or consumed by the buffer capacitor P_{B_n} is defined by the harvested power P_{EH_n} minus the power drawn by the load P_{MCU_n} . The load in this application includes only the MCU, and is related to the supply voltage V_{MCU} . It is essential to recognize that the MCU still consumes several microwatts of power at voltages below the threshold voltage $V_{MCU_{th}}$. If the voltage of 1.75 V is exceeded, P_{MCU} increases and the MCU starts executing instructions. Based on the power $P_{B_n} = P_{EH_n} - P_{MCU_n}$, the buffer capacitance C_B , and the voltage across the buffer capacitor at the previous time step $V_{B_{n-1}}$, the voltage V_{B_n} can be determined via

$$V_{B_n} = \begin{cases} 0, & V_{B_n} < 0 \\ V_{B_{n-1}}, & V_{EH_n} > V_{B_n}, P_{B_n} > 0 \\ \sqrt{V_{B_{n-1}}^2 + \frac{2P_{B_n}\Delta t}{C_B}}, & \text{else} \end{cases} \quad (4)$$

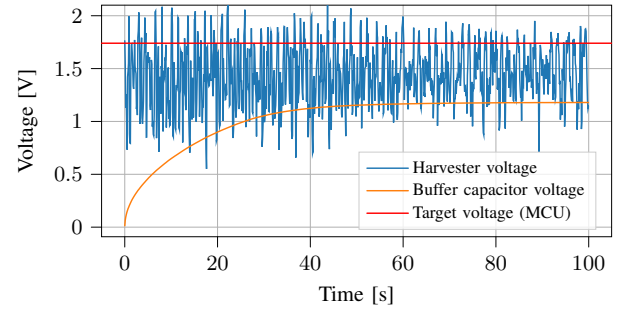
with P_{EH_n} depending on the incoming RF power $P_{RF_{in}}$ and P_{MCU_n} depending on $V_{B_{n-1}}$. The energy harvester output voltage V_{EH} changes over time and can drop below the voltage already present across the buffer capacitor, i.e., $V_{EH_n} < V_{B_n}$. When $V_{EH_n} > V_{B_n}$ and $P_{B_n} > 0$, the harvester is directly powering the MCU, keeping the buffer voltage unaltered as the voltage V_B cannot increase further due to an insufficient V_{EH} , i.e., $V_{B_n} = V_{B_{n-1}}$. Once the buffer voltage V_{B_n} reaches the MCU threshold voltage, sufficient energy is stored in the buffer to backscatter the pilot message. Furthermore, the response time can be estimated by calculating the buffer voltage progression. The calculations were applied to the measured data, available in [\[10\]](#) repository [10], resulting in the representations of the buffer voltage progression shown in Figs. 6a and 6b and discussed in detail below.³

2) *Response Time Results*: To obtain a realistic estimate of the response time, a Monte-Carlo simulation is run with the

³It may be observed that these calculations are not strictly necessary, as the buffer capacitance can be directly connected to the energy harvester. By consequently monitoring the buffer voltage over time, similar results can be obtained. However, the proposed approach facilitates a more comprehensive post-processing analysis. Suppose the pilot message, capacitor value or MCU load is changed, re-running the analyses immediately provides insights into the feasibility, charge time, and response time of the END.



(a) **Meas 1** Single-tone excitation.



(b) **Meas 2** Multi-tone excitation.

Fig. 6: Buffer voltage progression with USRP gain of 80 dB, corresponding to a total transmit power of 32.64 dBm (Table I), for **Meas 2**, the buffer never reaches the target voltage.

measured data. 50 random time instances are selected from the dataset and the time to charge the buffer is calculated according to Section IV-C1. Given that the MCU consumes power below the threshold, two configurations are considered, i.e., realistic⁴ and ideal MCU. In the ideal case, the MCU does not consume power below the threshold voltage. This specific case affect the response time calculations and shows that future ENDS incorporating reduced MCUs power consumption during periods of inactivity will have a significant impact on the results.

⁴The power consumption at different supply voltages of the MCU is measured and are available in [10].

The 50th percentile (P50) and 95th percentile (P95) values for the single-tone (**Meas 1**) and multi-tone (**Meas 2**) transmission for both the realistic and ideal MCU are summarized in Table II for different total transmit powers. From this, we can conclude that *for lower transmit powers, and in contrast to multi-tone, single-tone signals exceed the required threshold values, allowing to send a pilot signal*. Furthermore, Table II also shows that *lowering the power consumption of the MCU below $V_{MCU_{th}}$ allows to reduce the overall transmit power*.

Figure 7 plots the cumulative distribution function (CDF) of the response times over the 50 Monte-Carlo measurement-based simulations. It shows, that *while the single-tone has a higher spread of response times, it also has a higher probability of experiencing a shorter response time than the multi-tone signal*. This can be understood when inspecting Fig. 6, where multi-tone signals provide a more stable received DC power, while the adaptive single-tone exploits constructive interference over a longer time period as can be observed in Fig. 6a.

TABLE II: Computed 50th (P50) and 95th percentile (P95) of the END response time derived from single- and multi-tone measurements. Some configurations result in a response time exceeding the measurement time of 1 h, indicated by -.

Total transmit power [dBm]	Single-tone				Multi-tone			
	Realistic MCU P50 [s]	Realistic MCU P98 [s]	Ideal MCU P50 [s]	Ideal MCU P98 [s]	Realistic MCU P50 [s]	Realistic MCU P98 [s]	Ideal MCU P50 [s]	Ideal MCU P98 [s]
28.34	-	-	510	1159	-	-	-	-
29.20	-	-	418	756	-	-	-	-
30.06	-	-	206	389	-	-	-	-
30.92	620	1537	132	310	-	-	820	848
31.78	156	483	84	166	-	-	288	328
32.64	148	410	53	127	-	-	102	112
33.44	76	438	39	102	-	-	69	71
34.24	55	221	28	67	-	-	53	54
35.04	31	125	23	75	-	-	41	48
35.84	20	89	17	50	55	74	25	27
36.64	17	80	14	38	31	43	20	20

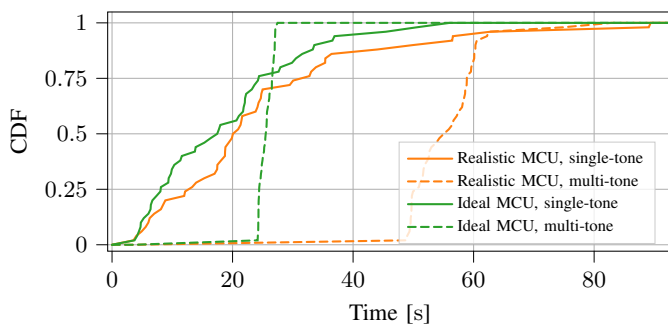


Fig. 7: CDF of the response times for a total transmit power of 35.84 dBm.

V. CONCLUSION

In this paper, we report and discuss various measurements at a static location within the Techtile testbed. It was found that, for the employed energy harvester, single-tone excitation yields the best results in terms of efficiency levels and END

response time. A fair comparison was achieved by evaluating the results using the same amount of radiated power. However, it was also observed that the response time amounts to several tens of seconds to backscatter just a 10-byte pilot signal. Future work should explore the analytical verification to prove that single-tone signals perform better in this particular case. Furthermore, the measurements will be repeated and multi-carrier transmission per antenna will be considered, as opposed to the current implementation. Also, the consumption of the inactive MCU could be reduced, as we have demonstrated that lowering the threshold voltage for the MCU leads to substantial performance improvements. There is also a broad spectrum of alternative options to the pure single-tone and multi-tone signals. Future investigations could explore whether different configurations of the infrastructure and, e.g., number of carriers, could yield performance gains. Moreover, the EP could be enhanced by integrating the buffer capacitor, allowing for more accurate validation of response time estimations.

The next step to support coherent downlink wireless power beamforming is capturing the backscatter uplink pilot signals and performing reciprocity-based downlink WPT beamforming (step 3 in Fig. 1).

REFERENCES

- [1] O. L. A. López *et al.*, “CSI-free vs CSI-based multi-antenna WET for massive low-power internet of things,” *IEEE Transactions on Wireless Communications*, vol. 20, no. 5, pp. 3078–3094, 2021.
- [2] B. J. B. Deutschmann *et al.*, “Location-based Initial Access for Wireless Power Transfer with Physically Large Arrays,” in *2022 IEEE International Conference on Communications Workshops (ICC Workshops)*, 2022, pp. 127–132.
- [3] M. Fujii, “Simple Transmit-Phase optimization for Focused-Beamforming Wireless Energy Transfer,” in *2022 IEEE 11th Global Conference on Consumer Electronics (GCCE)*, 2022, pp. 213–214.
- [4] A. Hajimiri *et al.*, “Dynamic Focusing of Large Arrays for Wireless Power Transfer and Beyond,” *IEEE Journal of Solid-State Circuits*, vol. 56, no. 7, pp. 2077–2101, Jul. 2021. (visited on 07/16/2024).
- [5] B. J. B. Deutschmann *et al.*, “XL-MIMO Channel Modeling and Prediction for Wireless Power Transfer,” in *2023 IEEE International Conference on Communications Workshops (ICC Workshops)*, 2023, pp. 1355–1361.
- [6] G. Callebaut *et al.*, “How to Perform Distributed Precoding to Wirelessly Power Shelf Labels: Signal Processing and Measurements,” in *2024 IEEE 25th International Workshop on Signal Processing Advances in Wireless Communications (SPAWC) (IEEE SPAWC 2024)*, Lucca, Italy, Sep. 2024, p. 4.97.
- [7] B. Clerckx *et al.*, “Low-Complexity Adaptive Multisine Waveform Design for Wireless Power Transfer,” *IEEE Antennas and Wireless Propagation Letters*, vol. 16, pp. 2207–2210, 2017.
- [8] M. S. Trotter *et al.*, “Power-optimized waveforms for improving the range and reliability of RFID systems,” in *2009 IEEE International Conference on RFID*, IEEE, 2009, pp. 80–87.
- [9] N. Shariati *et al.*, “Multitone excitation analysis in RF energy harvesters—Considerations and limitations,” *IEEE Internet of Things Journal*, vol. 5, no. 4, pp. 2804–2816, 2018.
- [10] J. Van Mulders *et al.*, *Scripts and Data – Single versus Multi-Tone Wireless Power Transfer with Physically Large Arrays*, <https://github.com/techtile-by-dramco/wpt-signals-for-initial-access/>, 2024.
- [11] G. Callebaut *et al.*, “Techtile—open 6G R&D testbed for communication, positioning, sensing, WPT and federated learning,” in *2022 Joint European Conference on Networks and Communications & 6G Summit (EuCNC/6G Summit)*, IEEE, 2022, pp. 417–422.
- [12] S. K. Divakaran *et al.*, “RF energy harvesting systems: An overview and design issues,” *International Journal of RF and Microwave Computer-Aided Engineering*, vol. 29, no. 1, 2019.